WEP
Warwick
Evans
Publishing

International Journal of Electric Power and Energy Studies
ISSN: 3006-0826 (Online) | Volume 1, Number 1, Year 2023
DOI: https://doi.org/10.62051/ijepes.v1n1.01
Journal homepage: https://wepub.org/index.php/IJEPES/index

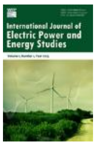

Study on the influence of processing technology on the properties of 2024-T3 aluminum alloy

Jin He, Hongfeng Feng and Pengjun Wen

School of Material Science and Engineering, Xi'an Shiyou University, Xian 710065, China

ABSTRACT

2024-T3 aluminum alloy is widely recognized for its low density and excellent mechanical properties. However, it has some shortcomings at high temperatures. Using Abaqus simulation technology, the surface heat source during the VIES (Variable Input Energy Source) treatment process was simulated, with the energy originating from the discharge channel. Through orthogonal experimental methods, it was indicated that the distribution and depth of the molten pool varied under different process parameters. Meanwhile, electric spark surface strengthening mainly affected the surface of the workpiece, with minimal impact on the internal structure. When the impact frequency is constant, increasing the input current enlarges the maximum heat flux density (Qmax) at the center, leading to an expansion of the molten pool area. Conversely, when the input current is constant, increasing the impact frequency shortens the contact time between the electric spark and the plate, resulting in reduced heat input from the electric spark. Consequently, the surface molten pool area decreases."

KEYWORDS

VIES; Surface heat source; Molten pool distribution; Heat flux density.

1. INTRODUCTION

In the aviation industry, to improve fuel efficiency and performance, aircraft structural materials must balance lightweight design and high strength. The 2024-T3 aluminum alloy, with its low density and excellent mechanical properties, has become the preferred material for lightweight aircraft structures. Additionally, its outstanding corrosion resistance in various climates and environmental conditions ensures the reliability and durability of aircraft.[1-3]. Despite the significant mechanical performance and corrosion resistance of 2024-T3 aluminum alloy in the aerospace industry, its performance is limited in high-temperature and high-pressure environments, especially under extreme conditions, where the alloy may become brittle, affecting its strength and toughness.[4-6].

To enhance its corrosion resistance, adopting surface strengthening techniques is an effective solution. Currently, there are various surface strengthening technologies available in the market, including high-energy beam heat treatment, chemical heat treatment, thermal spraying, cold spraying, micro-arc oxidation, laser cladding, chemical vapor deposition (CVD), physical vapor deposition (PVD), and shot peening, etc.7-12These methods significantly enhance the hardness and wear resistance of the material, extending its lifespan. However, these techniques typically involve complex operational processes, long processing cycles, and special operating environments, and require expensive equipment and higher costs. Therefore, we have developed an innovative surface strengthening technique - Vibration Impact Enhanced Sparking (VIES), which not only improves the corrosion resistance of the material but also is easy to operate and cost-effective. VIES integrates traditional vibration impact treatment and spark surface strengthening technology. The high-frequency forces generated by vibration impact improve the material's physical properties, and additional materials are fused to the workpiece surface during the spark discharge process, thereby enhancing surface quality [13-17].

This method not only optimizes the microstructure of the material surface and overall mechanical performance but also addresses the issues of melting zone and residual stress in traditional methods, significantly enhancing the material's fatigue resistance and stress corrosion resistance. To delve deeper into the mechanisms and performance of VIES technology, this study utilized Abaqus finite element software for analysis. This method can comprehensively analyze temperature field changes during vibration impact and electrical spark surface strengthening processes, laying a solid theoretical and data foundation for the future optimization and practical application of this technology.

2. FINITE ELEMENT EXPERIMENTAL DESIGN

2.1. Geometric Model

In the ABAQUS finite element simulation software, a three-dimensional geometric model was established based on the actual VIES process. The model consists of a hard alloy-made small sphere and a 2024-T3 aluminum alloy plate. The small sphere is a regular sphere with a diameter of 15mm; the plate is a square with a side length of 16mm and a height of 2mm. The schematic diagram of the geometric model is shown in Figure 1.

2.2. Thermal Model

During the VIES process, the surface heat source originates from the energy in the discharge channel and forms in the discharge region on the electrode surface, governing the surface enhancement process of electrical sparks.

The heat conduction process on the electrode surface is essentially a small-scale instantaneous surface heat source transferring heat to the interior of the electrode, thereby causing localized metal melting around the discharge points. The density of charged particles in the discharge channel is maximum at the axis, gradually decreasing along the radial direction, exhibiting a Gaussian distribution. Therefore, the heat flux density induced by high-temperature plasma also follows a Gaussian distribution. The heat source model used in this study is a Gaussian planar heat source, requiring only the determination of the maximum heat flux density Qmax at the center and the discharge channel radius R to determine the heat flux density.

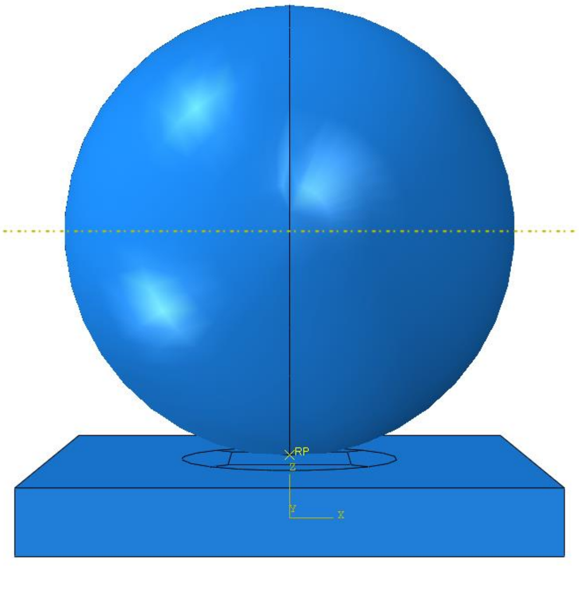

Figure 1. VIES Geometric Model

$$q(r)=q_{\max}\exp\left\{-4.5\times\left(\frac{r}{R}\right)^2\right\} \tag{1}$$

Maximum Heat Flux Density:

$$q_{\max}=\frac{4.5\times\eta\times U\times I}{\pi R^2} U=21.3, I=3.7, \eta=0.3 \tag{2}$$

Minimum Heat Flux Density1:

$$q_{\min}=0 \tag{3}$$

The discharge channel radius used in this study is:

$$R=0.788\times10^3\times t^{0.75} \tag{4}$$

In this study, a heat flux density subroutine "flux" was written in Fortran. It was used to apply heat flux density boundary conditions on the workpiece surface for the analysis and simulation of the transient temperature field in electrical discharge machining.

2.3. Thermal Boundary Conditions

To solve the exact temperature field distribution, this study assumes the workpiece is made of isotropic material. Additionally, it is necessary to determine the model's boundary conditions, initial temperature distribution, and the thermal properties of the material to accurately and concisely solve the temperature field in the process of vibration impact compound electrical discharge surface strengthening. In this process, considering the actual conditions of the research object, it is necessary to solve special solutions satisfying the heat conduction differential equation. To have a definite solution, practical boundary conditions for the heat transfer problem need to be set. The boundary conditions for the vibration impact compound electrical discharge surface strengthening include the initial temperature distribution at the initial moment (i.e., initial conditions) and the temperature or heat exchange conditions at the object's boundary (i.e., boundary conditions). The heat conduction differential equation, combined with initial and boundary conditions, fully describes a specific heat transfer problem. In vibration impact compound electrical discharge surface strengthening, the strengthening heat source is stationary. However, when the strengthening heat source vibrates up and down, the temperature, stress, and strain properties of the workpiece undergo rapid changes in time and space. At different moments and positions, the temperature distribution is extremely uneven. For the three-dimensional transient temperature field, the partial differential equation for the temperature variable (x, y, z, t) in Cartesian coordinates is:

$$\rho c\frac{\partial\theta}{\partial t}-\frac{\partial}{\partial x}\left[k_x\frac{\partial\theta}{\partial y}\right]-\frac{\partial}{\partial y}\left[k_y\frac{\partial\theta}{\partial y}\right]-\frac{\partial}{\partial z}\left[k_z\frac{\partial\theta}{\partial z}\right]-\Delta h(x,y,z)=0 \tag{5}$$

In the above equation, p represents the material density, c is the specific heat capacity of the material, and kx, ky, and kz are the thermal conductivity coefficients of the material in the x, y, and z directions, respectively. Ah(x, y, z) represents the material's heat generation. The boundary conditions of the heat transfer model reflect the thermal exchange between the material's outer surface and the surrounding environment. Heat conduction problems typically have three types of thermal boundary conditions: The first type is where the temperature or the distribution function of temperature on the workpiece boundary is known:

The second type is where the heat flux density qw on the material's surface is known, and the direction of the flow of heat flux density is specified along the outward normal f of the boundary:

$$-k(T)\frac{\partial T}{\partial \vec{n}} = q_w(x,y,z,t) \tag{6}$$

The third type is when the convective heat transfer coefficient h and the fluid temperature Tc between the workpiece material and the fluid in contact with it are known. This is also referred to as the Newtonian convective boundary:

$$-k(T)\frac{\partial T}{\partial \vec{n}}|_s = h(T_S - T_0) \tag{7}$$

The heat flux density of the spark strengthening process in a gas medium follows a Gaussian distribution and undergoes convective heat transfer with the surrounding flowing gas, hence falling under the second and third type of boundary conditions. The calculation region is chosen as a small cylindrical area around the discharge point on the surface of the workpiece, considering the workpiece as a semi-infinite body. Since the Gaussian distribution of the heat source is axisymmetric, the input of the heat flux density can be simplified into a two-dimensional model. A plane is created along the centerline of the heat flux distribution for a two-dimensional analysis, applying the heat flux to the surface of the workpiece. A portion of the heat is transferred to the upper surface through convective heat transfer, while the remaining heat is conducted into the workpiece. The left, right, and bottom surfaces away from the discharge point can be considered as regions without heat flow, i.e., at constant temperature. The boundary conditions of the heat transfer model can be represented in Figure 4.

2.4. Finite Element Orthogonal Test Plan

Table 1. Orthogonal test table of finite element analysis

Experiment number	Experimental scheme	Impulse frequency (A)f/ Hz	On-going current (B)I/A	Impact height (C)h/ mm
1	A1B1C1	20	30	0.010
2	A1B2C3	20	40	0.006
3	A1B3C2	20	50	0.008
4	A2B1C3	25	30	0.006
5	A2B2C2	25	40	0.008
6	A2B3C1	25	50	0.010
7	A3B1C2	40	30	0.008
8	A3B2C1	40	40	0.010
9	A3B3C3	40	50	0.006

The primary factors affecting the performance of 2024-T3 aluminum alloy are the electric current, impact frequency, and impact height, which are selected for orthogonal experiments. Based on actual experimental conditions and equipment parameter limitations, three levels were determined for each of the electric currents, impact frequencies, and impact heights. The three levels for electric current are 30A, 40A, and 50A; for impact frequency, they are 20Hz, 25Hz, and 40Hz; and for impact height, they are 0.06mm, 0.008mm, and 0.01mm, as detailed in Table 1.

3. NUMERICAL SIMULATION RESULTS AND DISCUSSION

3.1. VIES Finite Element Simulation Results and Analysis

In this spark discharge heat source, a pulsed form of energy input is employed. Taking the 2# experimental plan as an example, when the input current is 30A and the impact frequency is 20Hz, the total heat cycle is 5s. This includes a heating time of 0.025s and a cooling time of 4.975s. During the heating time of 0.025s, a pulsed heat input method is used. In the first quarter of the 0.025s, there is no heat input, from one-quarter to three-quarters, there is heat input, and from three-quarters onwards, there is no heat input until 5s, which represents the cooling time. The heat input for the 2# plan varies with time, as shown in Figure 2. The same principles apply to other spark discharge processing schemes. In this paper, a voltage setting of 20V is used, with a spark discharge heat source input efficiency of 0.85. The heat source radius is 3mm, and the melting point of the 2024-T3 aluminum alloy plate is 517℃.

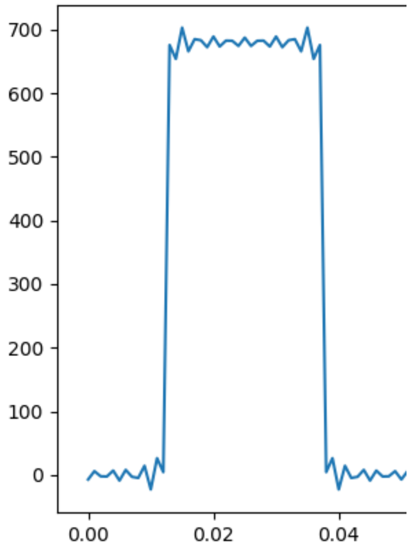

Figure 2. Thermal Input Variation Over Time for Scheme 2

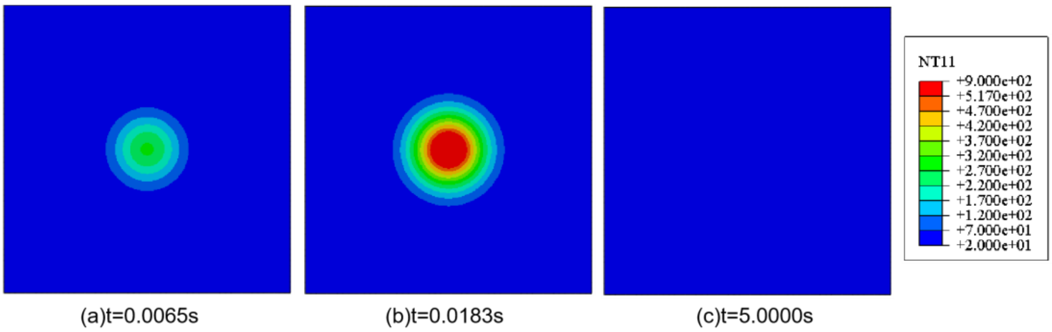

a.Surface Distribution Contour Maps of Electric Spark Temperature Field at Different Time Points

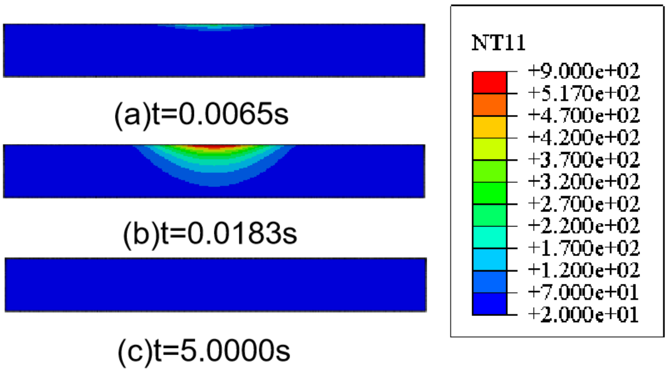

Figure 3. b: Y-Plane Cross-sectional Distribution Contour Maps of Electric Spark Temperature Field at Different Time Points

Figure 3 shows the temperature field distribution contour map of the joint at different welding moments under the spark discharge process parameters of 40A electric current and 20Hz impact frequency. From the figure, it can be observed that, unlike the arc pool surface moving in a shape similar to a top-down view of an egg, the surface of the stationary arc pool forms a circular pool. The temperature distribution contour lines of the longitudinal cross-section of the pool are roughly elliptical. At the center of the arc, the pool temperature is highest, with a greater depth of fusion. Outside the center of the arc, the pool temperature is relatively lower, with a small decrease in temperature in the adjacent range, followed by a rapid decrease. It can be seen that the highest temperature occurs on the surface of the workpiece, indicating that spark discharge surface strengthening mainly affects the surface layer of the workpiece, with minimal impact on the interior. Influenced by the heating process, it is evident that spark discharge surface strengthening has the characteristic of rapid heating and cooling.

3.2. Analysis of Orthogonal Experimental Results

Figure 5 shows the cross-sectional temperature field distribution of the flat plate under different spark discharge process parameters, with the contour map distribution forming an elliptical shape under the combined action of input current and impact frequency. In each row of the cross-sectional temperature distribution contour map, from left to right, the pool area gradually increases, the width increases, and the thickness direction also increases; in each column from top to bottom, the pool area gradually decreases, the width decreases, and the thickness direction also decreases. The pool area in Figures 5(a), (b), and (c) increases sequentially, indicating that at a constant impact frequency, as the input current increases, the maximum heat flux density Qmax at the center increases, causing the pool area to increase. When the input current is constant, from Figures 5(a), (d), (g), it can be seen that with the increase of impact frequency, the spark discharge heating process has a shorter contact time with the flat plate, resulting in a decrease in spark discharge heat input, hence reducing the surface pool area.

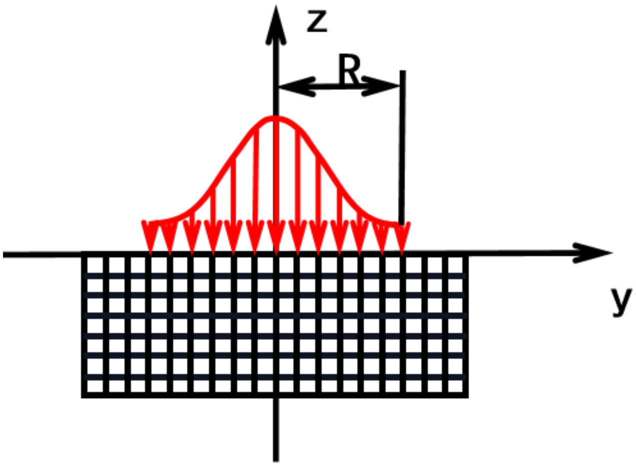

Figure 4. Boundary conditions of the heat source model

According to relevant literature, a melt pool depth of approximately 200 micrometers is generally considered optimal. Considering the superior bonding between 2024-T3 aluminum alloy and in-situ generated aluminum nitride compared to typical metal/non-metal combinations. However, even with a melt pool set at 200 micrometers, there remains a significant risk of large-area detachment, as evidenced by preliminary experiments conducted by the author. Therefore, considering this, a melt pool depth ranging from 100 to 150 micrometers is defined as an optimal melt pool interval. Specifically, within the range of 100 to 150 micrometers, a score increases as it approaches 150 micrometers; melt pools smaller than 100 micrometers or larger than 150 micrometers are categorized as suboptimal, with scores decreasing accordingly. A score of zero is assigned to the absence of a melt pool or when the melt pool is indistinct. The detailed scoring criteria are provided in Table 2 for reference.

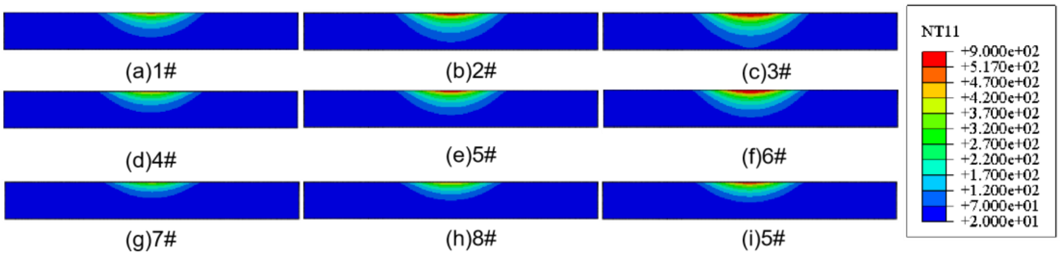

Figure 5. Cloud diagram of molten pool distribution under different EDM process parameters

Table 2. Score of EDM pool with different parameters

Experiment number	Experimental scheme	Impulse frequency f/ Hz	On-going current I/A	Molten pool h/ mm	Molten pool score
1	A1B1C1	20	30	0.011	50
2	A1B2C3	20	40	0.132	90
3	A1B3C2	20	50	0.228	70
4	A2B1C3	25	30	0.000	0
5	A2B2C2	25	40	0.084	50
6	A2B3C1	25	50	0.176	80
7	A3B1C2	40	30	0.000	0
8	A3B2C1	40	40	0.011	50
9	A3B3C3	40	50	0.068	60

Based on the above analysis, the results of the orthogonal experimental design are as follows: the optimal process parameters are in Scheme 2; the intermediate process parameters are in Scheme 5; the least favorable process parameters are in Schemes 4 and 2.

4. SUMMARY

This paper focuses on the key factors influencing the performance of 2024-T3 aluminum alloy, primarily electric current, impact frequency, and impact height. Experimental design and finite element analysis were conducted using the orthogonal experimental method. The experimental results indicate differences in the distribution and depth of the melt pool under different process parameters. In-depth analysis of the experimental results identified optimal, intermediate, and poor process parameter schemes. This paper also elaborates on the simulation results of the electrical spark heat source and temperature field distribution, as well as the rating criteria for the melt pool. In the comprehensive analysis of the results, the optimal process parameter scheme is A1B2C3, the intermediate scheme is A2B2C2, and the poorest schemes are A2B1C3 and A3B1C2. Overall, this study provides beneficial references for optimizing the processing technology of 2024-T3 aluminum alloy.

REFERENCES

[1] Li C, Zhang D, Gao X, et al. Numerical simulation and experimental research on friction stir welding of 2024-T3 aeronautical aluminum alloy. Journal of Adhesion Science and Technology 2021, 35, 1-19.

[2] Xiao X, Zhou Z, Liu C, et al. Microstructure and Its Effect on the Intergranular Corrosion Properties of 2024-T3 Aluminum Alloy Crystals [Online], 2022.

[3] Huda Z, Zaharinie T, Kinetics of grain growth in 2024-T3: An aerospace aluminum alloy. Journal of Alloys and Compounds 2009, 478 (1), 128-132.

[4] Sancho, R, Cendón D, Gálvez F, Mechanical Behaviour of Al2024-T3 Sheet Metal at Different Strain-rates and Temperatures. Procedia Engineering 2017, 197, 158-167.

[5] Ampazis N, Alexopoulos N D, In Prediction of Aircraft Aluminum Alloys Tensile Mechanical Properties Degradation Using Support Vector Machines, Springer Berlin Heidelberg: Berlin, Heidelberg, 2010; pp 9-18.

[6] Klosak, M.; Santiago, R.; Jankowiak, T.; et al. The Influence of Temperature in the Al 2024-T3 Aluminum Plates Subjected to Impact: Experimental and Numerical Approaches. Materials (Basel) 2021, 14 (15).

[7] Zhang Y, Strengthening, Corrosion and Protection of High-Temperature Structural Materials. Coatings 2022, 12 (8), 1136.

[8] Wei X X, Zhang B, Wu B, et al. Enhanced corrosion resistance by engineering crystallography on metals. Nature Communications 2022, 13 (1), 726.

[9] Singh S, Kumar S, Khanna V, A review on surface modification techniques. Materials Today: Proceedings 2023.

[10] Liu H, Meng T L, Cao J, et al. In Advanced Surface Engineering and Protective Coating, Proceedings of the 2nd International Conference on Advanced Surface Enhancement (INCASE 2021), Singapore, 2022//; Wei, Y.; Chng, S., Eds. Springer Singapore: Singapore, 2022; pp 138-141.

[11] Sun Y, Surface Engineering & Coating Technologies for Corrosion and Tribocorrosion Resistance. Materials (Basel) 2023, 16 (13).

[12] Chen Y, Zhang, X, Ding D, et al. Integration of interlayer surface enhancement technologies into metal additive manufacturing: A review. Journal of Materials Science & Technology 2023, 165, 94-122.

[13] Paustovskii A V, Gubin Y V, Stresses in coatings obtained by electro-spark alloying and laser processing (review). Materials Science 1997, 33 (6), 770-776.

[14] Mashkov Y K, Korotaev D N, Alimbaeva B S, The effect of electric-spark treatment on the structure and properties of modified friction surfaces. Journal of Friction and Wear 2016, 37 (1), 66-70.

[15] Spadlo S, Bankowski D, Mlynarczyk, P, Research on the impact of vibratory machining on the layer applied with the ESD technique. Mechanik 2018.

[16] Wei X, You-Xi L, Ze-Feng X, Research and Development of the Electro-spark Surface Strengthening Technology. Development and Application of Materials 2011.

[17] Sayfullin R N, Gaskarov I R, Pavlov N I, Improvement of electric spark surfacing method. 2020.